Supporting Information

A strongly coupled oxide-support heterostructure for efficient acidic water oxidation

Hongjun Chen,[a] Liming Deng,[a] Shuyi Liu,[a] Feng Hu,*[a] Linlin Li,*[a] Jianwei Ren[c] and Shengjie Peng*[ab]

[a] College of Materials Science and Technology, Nanjing University of Aeronautics and Astronautics, Nanjing 210016, China

E-mail: fenghu@nuaa.edu.cn (Feng Hu), lilinlin@nuaa.edu.cn (Linlin Li), pengshengjie@nuaa.edu.cn (Shengjie Peng)

[b] State Key Laboratory of High Performance Ceramics and Superfine Microstructure, Shanghai 200050, China

[c] Department of Chemical Engineering, University of Pretoria, cnr Lynnwood Road and Roper Street, Hatfield 0028, South Africa

Email: jianwei.ren@up.ac.za (Jianwei Ren)

1. Experimental Section

1.1 Materials

Manganese chloride tetrah ($MnCl_2·4H_2O$, 99%), cobalt chloride hexahydrate ($CoCl_2·6H_2O$, 99.7%), carbamide ($(NH_2)_2CO$, 99%), ruthenium trichloride ($RuCl_3$, 99.9%), and polyvinylidene fluoride (PVDF, 99%) were obtained from Aladdin (Shanghai, China).

1.2 Synthesis of $MnCo_2O_{4.5}$

198 mg of $MnCl_2·4H_2O$, 600 mg of carbamide, and 476 mg of $CoCl_2·6H_2O$ were evenly dispersed in 40 mL of deionized water. After stirring the solution thoroughly, the solution was transferred to an autoclave. Then, the autoclave was placed in an oven and reacted at 120°C for 16 h. Subsequently, the $MnCo(OH)_x$ product was rinsed with deionized water and anhydrous ethanol multiple times, and dried in an vacuum-drying oven at 60°C. Finally, the $MnCo(OH)_x$ was calcined in a muffle furnace at 400°C for 3 h to obtain $MnCo_2O_{4.5}$ powder.

1.3 Synthesis of $RuO_2/MnCo_2O_{4.5}$

40 mg of $RuCl_3$ and 40 mg of $MnCo_2O_{4.5}$ were evenly dispersed in 30 mL of deionized water and stirred thoroughly for 2 h. The mixed solution was rinsed with deionized water and anhydrous ethanol alternately, and dried in an vacuum-drying oven at 60°C to obtain the $RuO_2/MnCo_2O_{4.5}$ precursor powder. The $RuO_2/MnCo_2O_{4.5}$ was calcined in a muffle furnace at 350°C for 3 h. $RuO_2/MnCo_2O_{4.5}$-1, $RuO_2/MnCo_2O_{4.5}$-2 were prepared with the different mass ratios of $RuCl_3$ to $MnCo_2O_{4.5}$ as 1:2 and 3:2, respectively.

1.4 Characterization

X-ray diffraction (XRD) data acquired from the Bruker D8 advance (Billerica) with a guaranteed scanning rate of 10° min^{-1} was used to explore the crystal structure. The morphology and microstructure observations were made using a scanning electron microscope (SEM, Regulus 8100). Transmission electron

microscope (TEM) data was obtained on FEI Tecnai G2 F20. The valence state of the catalyst was measured and analyzed by X-ray photoelectron spectrometer (XPS Escalab 250Xi). Electron paramagnetic resonance (EPR) tests were performed using the EMX-6/1 instrument to indentify the oxygen vacancies. The extended X-ray absorption fine structure (EXAFS) was measured at the Beijing Photon Source (easyXAFS300, easyXAFS LLC) beamline. In-situ Raman spectroscopy were collected on a confocal Raman spectroscopy system, which is constructed by the SmartRaman confocal module and the HORIBA iHR550 spectrometer, with a 532 nm laser wavelength and a 50× long-focus microscope lens. In situ Raman spectroscopy measurements were conducted in a custom flow-type in situ Raman electrochemical cell. Before the experiment, the Raman spectroscopy system was calibrated using a standard silicon wafer (520.7 cm^{-1}).

1.5 Electrochemical measurements

The catalyst, conductive agent (carbon black), and binder (polyvinylidene fluoride, PVDF) were mixed at a mass ratio of 7:2:1 to obtain the catalyst paste. The working electrode was made by coating the slurry on 1×1 cm^2 nickel foam. A standard three-electrode system was used to test the electrocatalytic activity of the catalyst at the Electrochemical Workstation (Autolab Instrument). The prepared catalyst was used as the working electrode, graphite rod was used as the counter electrode (CE), and a KCl-saturated Ag/AgCl electrode was used as the reference electrode (RE) for the HER tests. All potentials in the work reported were converted relative to the reversible hydrogen electrode (RHE) according to the Nernst equation ($E_{RHE} = E_{Ag/AgCl} + 0.197 + 0.0591 \times pH$). Polarization curves were measured by linear sweep voltammetry (LSV) at a scan rate of 5 mV s^{-1} and compensated using iR. Electrochemical surface area (ECSA) was obtained by measuring capacitance at scan rates of 20~140 mV s^{-1}. The electrochemical impedance spectroscopy (EIS) was conducted over the frequency range of 0.01~10^5 kHz with an amplitude of 10 mV.

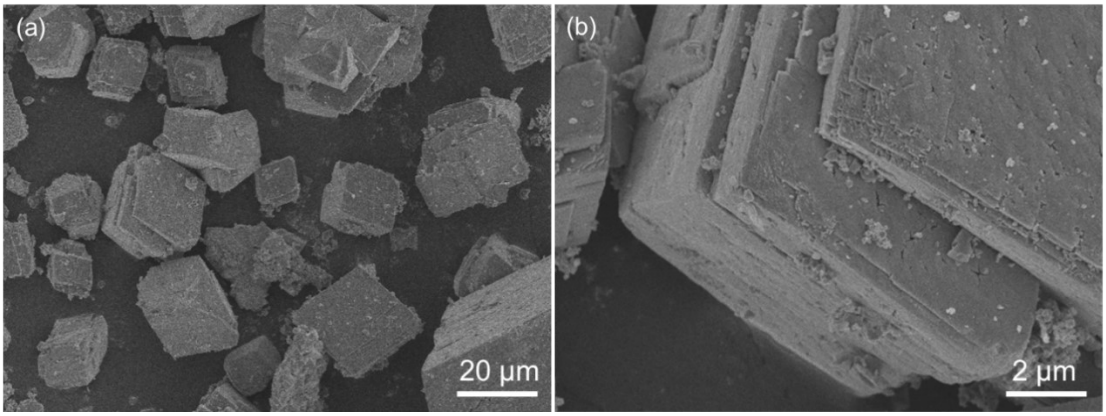

Fig. S1 (a) High-power; (b) low-power SEM images of $MnCo_2O_{4.5}$.

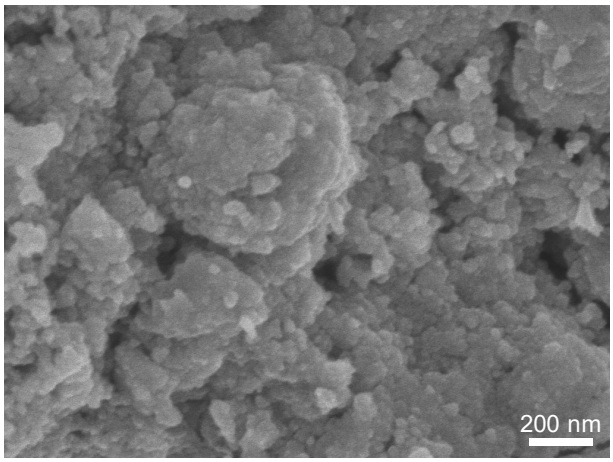

Fig. S2 SEM image of $RuO_2/MnCo_2O_{4.5}$.

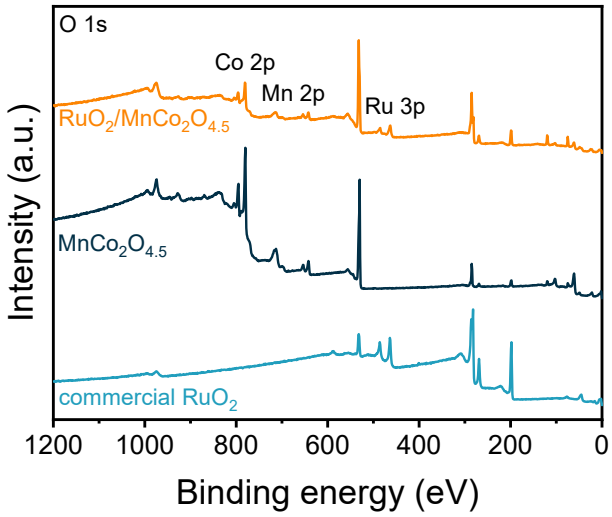

Fig. S3 The wide XPS wide-scan for $RuO_2/MnCo_2O_{4.5}$, $MnCo_2O_{4.5}$ and commercial RuO_2, respectively.

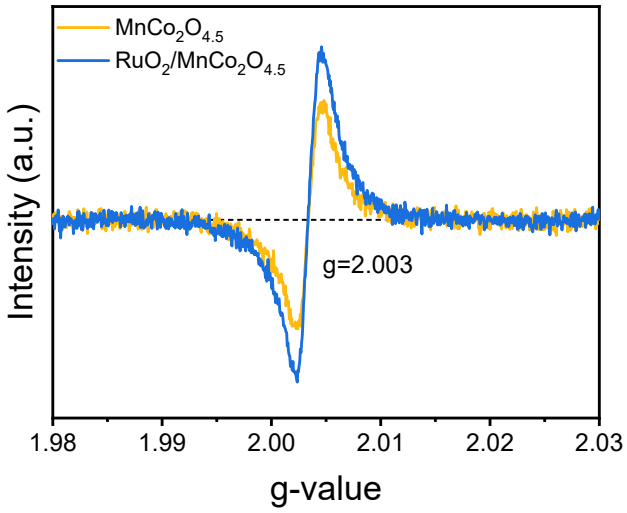

Fig. S4 EPR spectra of $MnCo_2O_{4.5}$ and $RuO_2/MnCo_2O_{4.5}$, respectively.

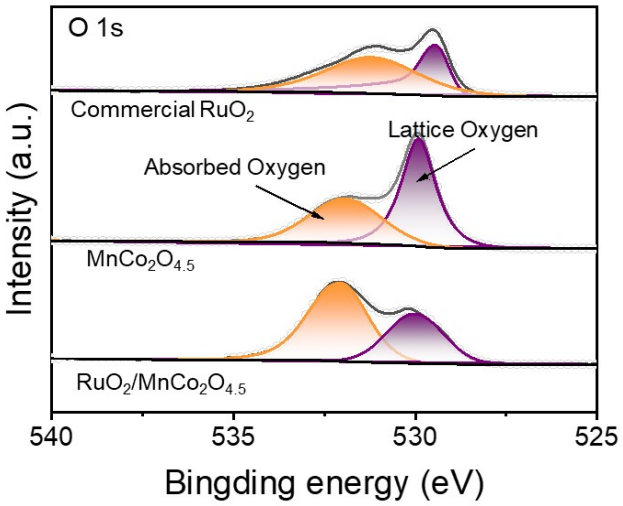

Fig. S5 O 1s XPS spectra of $RuO_2/MnCo_2O_{4.5}$, $MnCo_2O_{4.5}$ and commercial RuO_2, respectively.

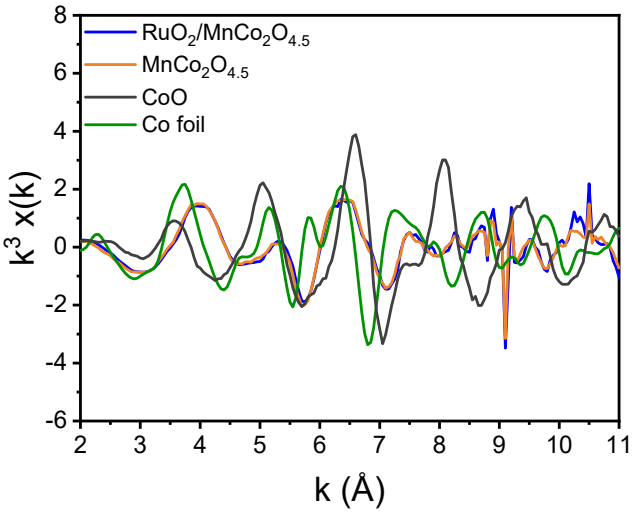

Fig. S6 Co K-edge EXAFS oscillation function of Co foil, CoO, $MnCo_2O_{4.5}$ and $RuO_2/MnCo_2O_{4.5}$, respectively.

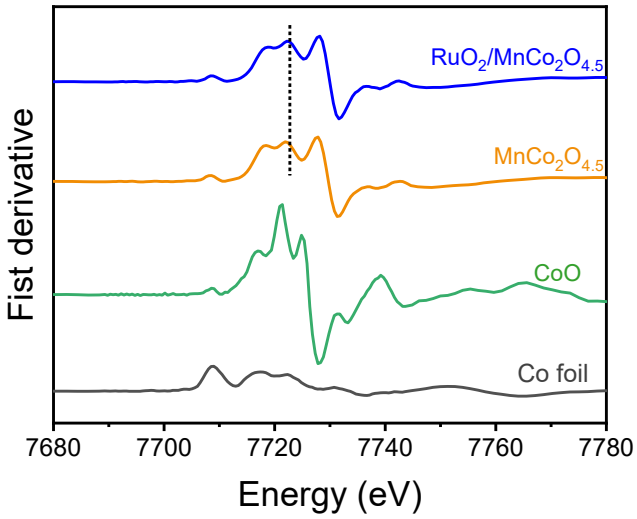

Fig. S7 The first derivative spectra of Co foil, CoO, $MnCo_2O_{4.5}$ and $RuO_2/MnCo_2O_{4.5}$, respectively.

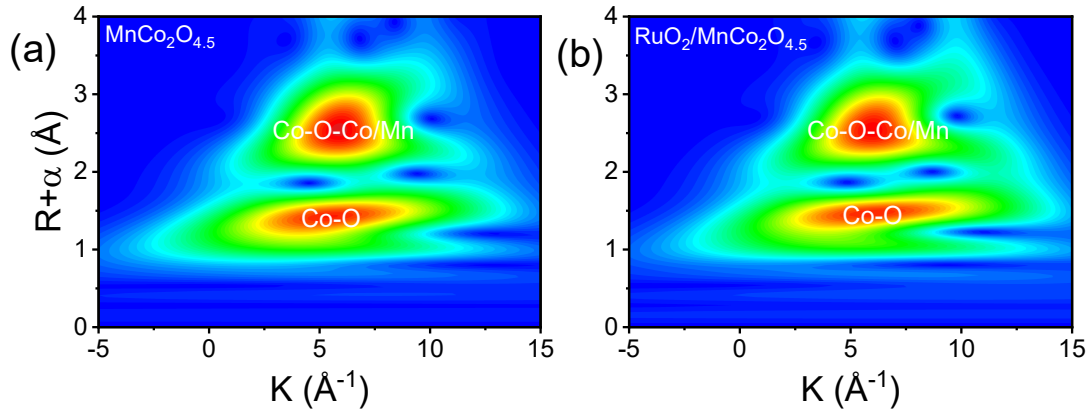

Fig. S8 WT of the Co K-edge for $MnCo_2O_{4.5}$ and $RuO_2/MnCo_2O_{4.5}$, respectively.

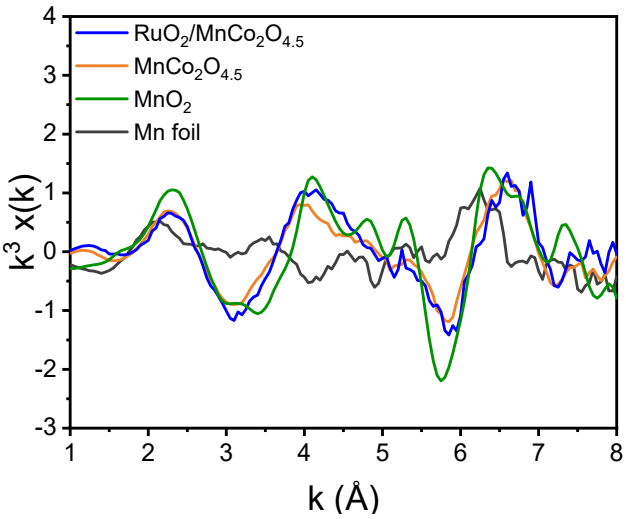

Fig. S9 Mn K-edge EXAFS oscillation function of Mn foil, MnO_2, $MnCo_2O_{4.5}$ and $RuO_2/MnCo_2O_{4.5}$, respectively.

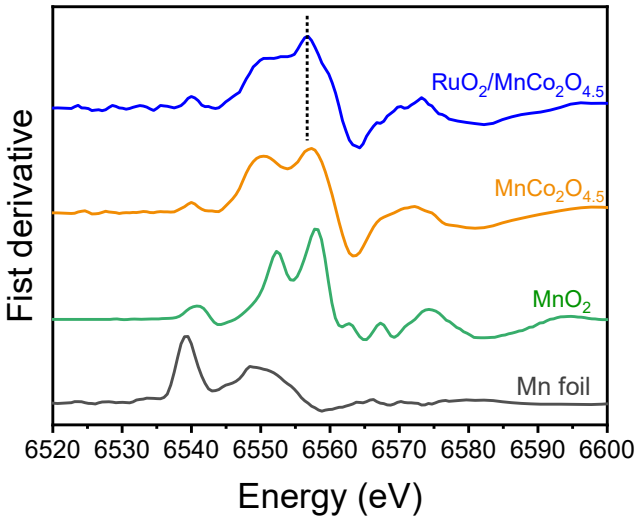

Fig. S10 The first derivative spectra of Mn foil, MnO_2, $MnCo_2O_{4.5}$ and $RuO_2/MnCo_2O_{4.5}$, respectively.

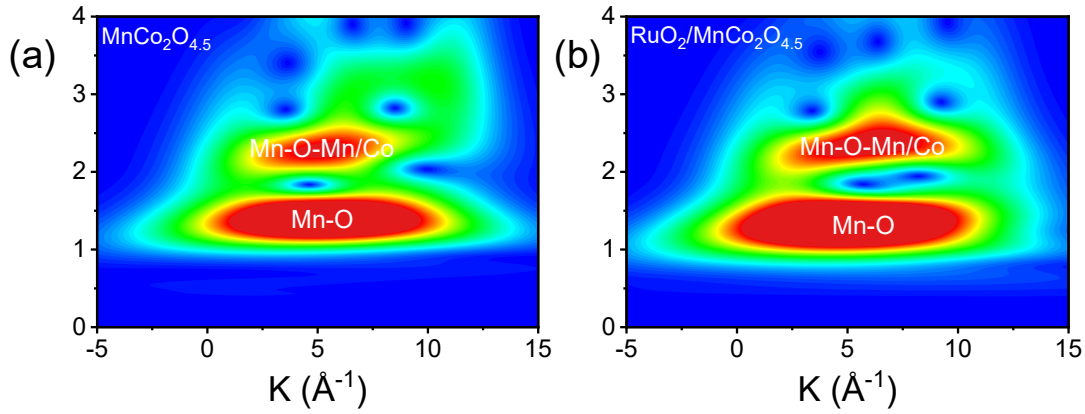

Fig. S11 WT of the Mn K-edge for $MnCo_2O_{4.5}$ and $RuO_2/MnCo_2O_{4.5}$, respectively.

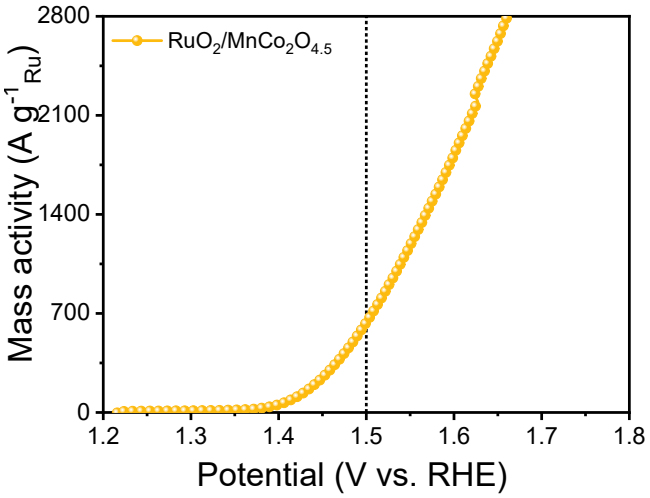

Fig. S12 The Ru mass normalized LSV curves of $RuO_2/MnCo_2O_{4.5}$.

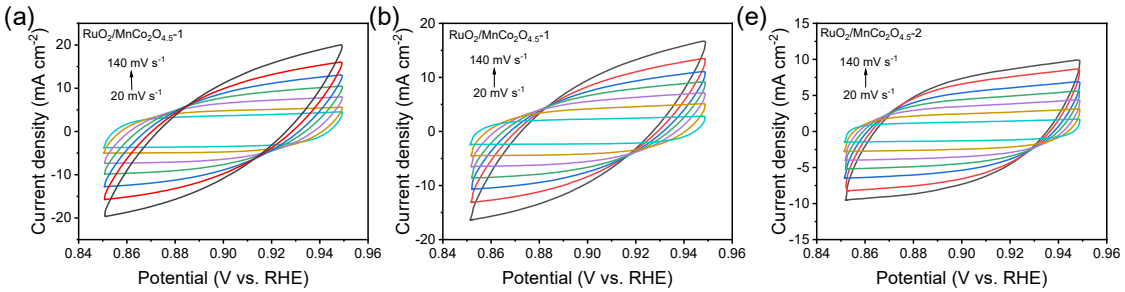

Fig. S13 The CV curves of (a) $RuO_2/MnCo_2O_{4.5}$, (b) $RuO_2/MnCo_2O_{4.5}$-1, and (c) $RuO_2/MnCo_2O_{4.5}$-2 at various scan rates, respectively.

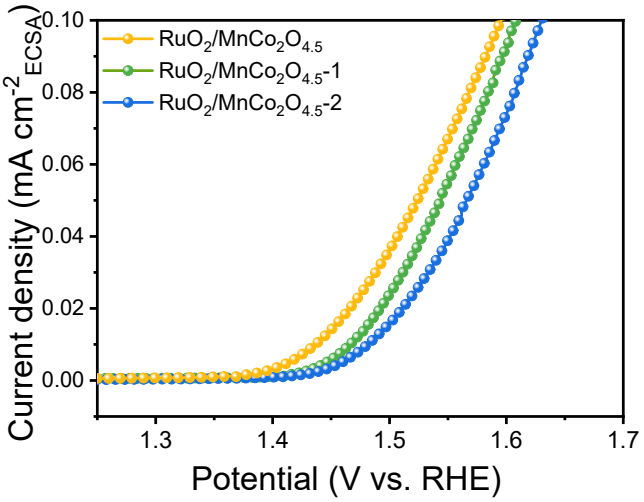

Fig. S14 The OER polarization curves normalized by the ECSA for $RuO_2/MnCo_2O_{4.5}$, $RuO_2/MnCo_2O_{4.5}$-1, and $RuO_2/MnCo_2O_{4.5}$-2.

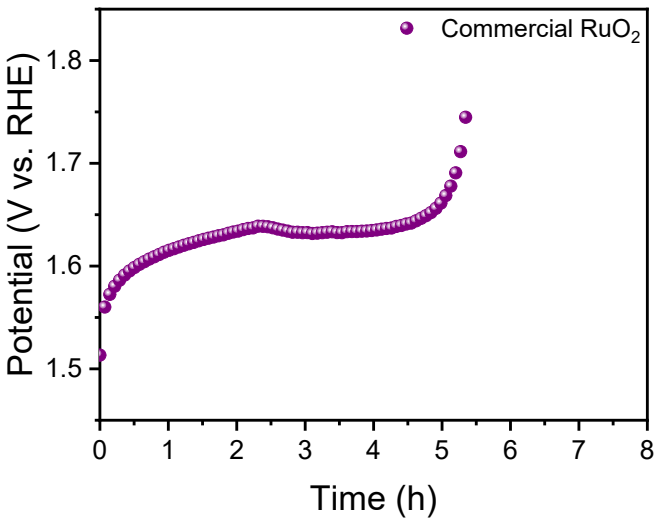

Fig. S15 Stability diagram of commercial RuO_2 in a three-electrode system.

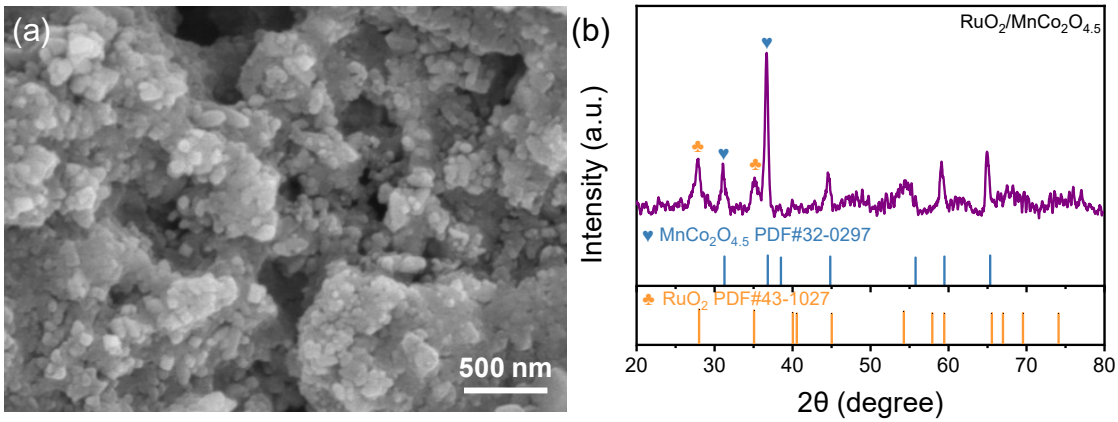

Fig. S16 (a) SEM, and (b) XRD images of $RuO_2/MnCo_2O_{4.5}$ after OER test.

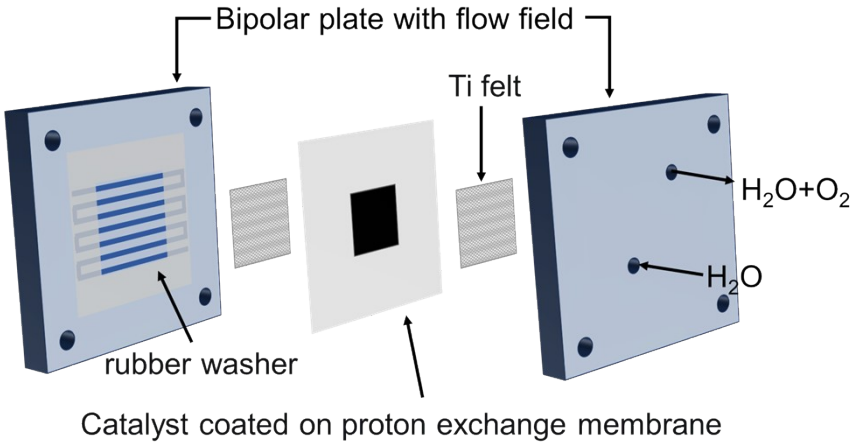

Fig. S17 Schematic diagram of the composition of the PEM electrolyzer.

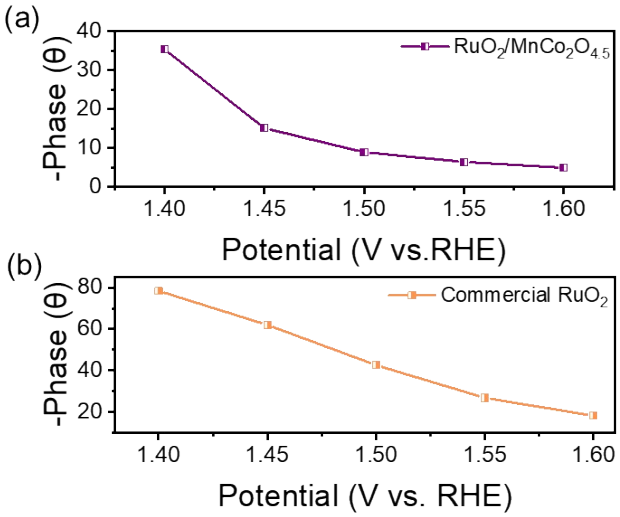

Fig. S18 Response of the R_{ct} charge transfer resistance to the applied potential of (a) $RuO_2/MnCo_2O_{4.5}$ and (b) commercial RuO_2.

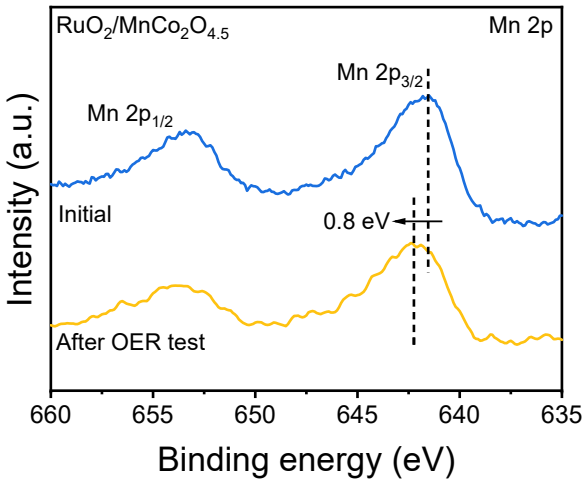

Fig. S19 Mn 2p XPS spectra of $RuO_2/MnCo_2O_{4.5}$ before and after OER test.

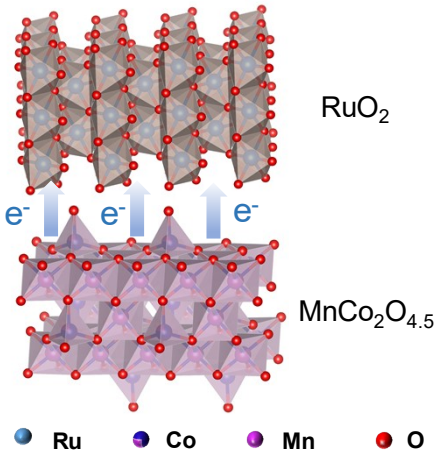

Fig. S20 Schematic illustrations of the electron supply effect in $RuO_2/MnCo_2O_{4.5}$.

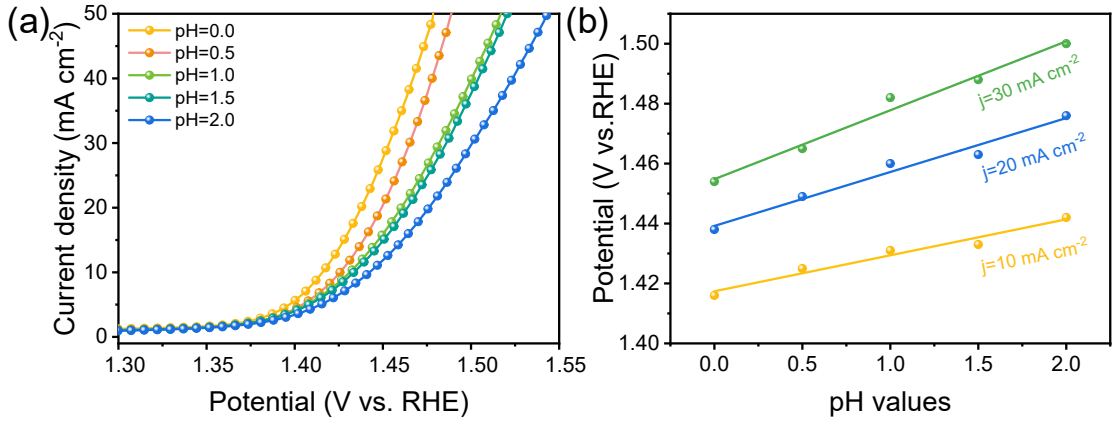

Fig. S21 (a) LSV curves of $RuO_2/MnCo_2O_{4.5}$ in electrolytes of different pH values. (b) pH dependence on the OER potential at 10, 20, and 30 mA cm^{-2} for $RuO_2/MnCo_2O_{4.5}$.

Table S1. Comparison table of overpotential and stability of different Ru-based catalysts in acidic electrolyte.

Catalyst	Overpotential @10mA cm^{-2}	Stability(h)	Reference
$RuO_2/MnCo_2O_{4.5}$	**190**	**150**	**This Work**
Ru@V-RuO_2/C HMS	237	15	Adv. Mater. 2023, 35, e2206351
Ru/Se/RuO_2	190	24	Adv. Funct. Mater., 2023, 33, 2211102
2D-RuO_2/G	169	/	Nano Energy, 2020, 78, 105185
1D-RuO_2-CN_x	250	50	ACS Appl. Mater. Inter., 2016. 8. 28678-28688
RuO_2/D-TiO_2	180	30	ACS Catal., 2022, 12, 9437-9445
s-RuO_2/ATO	198	12	Adv. Sci., 2022, 9, 2201654
H/d-MnO_x/RuO_2	178	40	Adv. Funct. Mater., 2023, 33, 2307010
RuO_2-WC NPs	347	10	Angew. Chem. Int. Ed. Engl., 2022, 61, e202202519
CoO_x/RuO_x-CC	180	60	Small, 2023, 19, e2302238
$Ru_{0.6}Cr_{0.4}O_2$	195	20	Small Methods, 2022, 6. 2200636
RuO_2/$(Co,Mn)_3O_4$/CC	270	24	Appl. Catal. B Environ., 2021, 297, 120442
RuB_2	223	10	ACS Energy Lett., 2020, 5, 2909

Table S2. Comparison table of mass activity of different Ru-based catalysts in acidic electrolyte.

Catalyst	Mass activity ($A\ g^{-1}$)	Reference
$RuO_2/MnCo_2O_{4.5}$	**636@270 mV 1515.7@347 mV**	**This Work**
$Cr_{0.6}Ru_{0.4}O_2$(550)	229@270 mV	Nat. Commun., 2019, 10, 162
RuO_2-WC NPs	1430@347 mV	Angew. Chem. Int. Ed. Engl., 2022, 61, e202202519
$Ru_{0.6}Cr_{0.4}O_2$	46.71@270 mV	Small Methods, 2022, 6, 2200636
RuO_2/SnO_2-xX	115.2@200 mV	Small, 2023, 19, 2301516
$Re_{0.06}Ru_{0.94}O_2$	500@272 mV	Nat. Commun., 2023, 14, 354
py-RuO_2:Zn	100@212 mV 800@300 mV	Nat. Commun., 2023, 14, 2517
RuO_2/MnO_2/CC	229.67@250 mV	Small, 2024, 20, 2310464
$RuO_2/(Co,Mn)_3O_4$/CC	366.5@300 mV	Appl. Catal. B Environ., 2021, 297, 120442

Table S3. Comparison table of overpotential and stability of different Ru-based catalysts in acidic PEMWE.

Catalyst	Potential (V)	Stability (h)	Reference
$RuO_2/MnCo_2O_{4.5}$	**1.76@500 mA cm^{-2} 1.98@1000 mA cm^{-2}**	**50 @200 mA cm^{-2}**	**This Work**
$W_{0.2}Er_{0.1}Ru_{0.7}O_{2-\delta}$	/	120 @100 mA cm^{-2}	Nat. Commun., 2020, 11. 5368
$Nd_{0.1}RuO_x$/CC	1.595@50 mA cm^{-2}	50 @10 mA cm^{-2}	Adv. Funct. Mater., 2023, 33. 2213304
PtCo–RuO_2/C,	1.6@1000 mA cm^{-2}	24 @1000 mA cm^{-2}	Energ Environ Sci., 2022, 15, 1119-1130
SS Pt-RuO_2 HNSs	/	100 @100 mA cm^{-2}	Sci. Adv., 2022, 8, 9271
RuO_2/SnO_2-1.5X	1.52@500 mA cm^{-2} 1.6@1000 mA cm^{-2}	30 @500 mA cm^{-2}	Small, 2023, 19. 2301516
$Ru_{0.6}Cr_{0.4}O_2$	/	12 @100 mA cm^{-2}	Small Methods, 2022, 6. 2200636
a/c-RuO_2	1.52@10 mA cm^{-2}	20 @50 mA cm^{-2}	Angew. Chem. Int. Ed., 2021, 60, 18821-18829
CoO_x/RuO_x-CC	1.64@100 mA cm^{-2}	100 @100 mA cm^{-2}	Small, 2023, 19, e2302238
Ir-MnO_2(160)-CC	1.65@100 mA cm^{-2}	70 @100 mA cm^{-2}	Adv. Sci., 2023, 2205920